


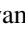



Discovery of Dying Active Galactic Nucleus in Arp 187: Experience of Drastic Luminosity Decline within 104 yr

著者	Kohei Ichikawa, Junko Ueda, Hyun-Jin Bae, Taiki Kawamuro, Kenta Matsuoka, Yoshiki Toba, Megumi Shidatsu
journal or publication title	The Astrophysical Journal
volume	870
number	65
page range	1-12
year	2019-01-09
URL	http://hdl.handle.net/10097/00126935

doi: 10.3847/1538-4357/aaf233



Discovery of Dying Active Galactic Nucleus in Arp 187: Experience of Drastic Luminosity Decline within 10^4 yr

Kohei Ichikawa^{1,2,3} , Junko Ueda^{4,5}, Hyun-Jin Bae⁶ , Taiki Kawamuro^{4,13} , Kenta Matsuoka^{7,8,9,13} ,
Yoshiki Toba^{9,10,11,13} , and Megumi Shidatsu¹²

¹ Frontier Research Institute for Interdisciplinary Sciences, Tohoku University, Sendai 980-8578, Japan; k.ichikawa@astr.tohoku.ac.jp

² Department of Astronomy, Columbia University, 550 West 120th Street, New York, NY 10027, USA

³ Department of Physics and Astronomy, University of Texas at San Antonio, One UTSA Circle, San Antonio, TX 78249, USA

⁴ National Astronomical Observatory of Japan, 2-21-1 Osawa, Mitaka, Tokyo 181-8588, Japan

⁵ Harvard-Smithsonian Center for Astrophysics, 60 Garden Street, Cambridge, MA 02138, USA

⁶ Department of Medicine, University of Ulsan College of Medicine, Seoul 05505, Republic Of Korea

⁷ Dipartimento di Fisica e Astronomia, Università degli Studi di Firenze, Via G. Sansone 1, I-50019 Sesto Fiorentino, Italy

⁸ INAF—Osservatorio Astrofisico di Arcetri, Largo Enrico Fermi 5, I-50125 Firenze, Italy

⁹ Research Center for Space and Cosmic Evolution, Ehime University, 2-5 Bunkyo-cho, Matsuyama, Ehime 790-8577, Japan

¹⁰ Academia Sinica Institute of Astronomy & Astrophysics (ASIAA), 11F of Astronomy-Mathematics Building, AS/NTU, No.1, Section 4, Roosevelt Road, Taipei 10617, Taiwan

¹¹ Department of Astronomy, Kyoto University, Kitashirakawa-Oiwake-cho, Sakyo-ku, Kyoto 606-8502, Japan

¹² Department of Physics, Faculty of Science, Ehime University, Matsuyama 790-8577, Japan

Received 2018 August 15; revised 2018 November 2; accepted 2018 November 18; published 2019 January 9

Abstract

Arp 187 is one of the fading active galactic nuclei (AGNs), whose AGN activity is currently decreasing in luminosity. We investigate the observational signatures of AGN in Arp 187, which trace various physical scales from less than 0.1 pc to the nearly 10 kpc, to estimate the long-term luminosity change over 10^4 yr. The Very Large Array 5 GHz and 8 GHz images and the ALMA 133 GHz images reveal bimodal jet lobes with ~ 5 kpc size and the absence of the central radio core. The 6dF optical spectrum shows that Arp 187 hosts a narrow line region with the estimated size of ~ 1 kpc, and the line strengths give the AGN luminosity of $L_{\text{bol}} = 1.5 \times 10^{46}$ erg s $^{-1}$. On the other hand, the current AGN activity estimated from the AGN torus emission gives the upper bound of $L_{\text{bol}} < 2.2 \times 10^{43}$ erg s $^{-1}$. The absence of the radio core gives the more strict upper bound of the current AGN luminosity of $L_{\text{bol}} < 8.0 \times 10^{40}$ erg s $^{-1}$, suggesting that the central engine is already quenched. These multiwavelength signatures indicate that Arp 187 hosts a “dying” AGN: the central engine is already dead, but the large-scale AGN indicators are still observable as the remnant of the past AGN activity. The central engine has experienced the drastic luminosity decline by a factor of $\sim 10^{3-5}$ fainter within $\sim 10^4$ yr, which is roughly consistent with the viscous timescale of the inner part of the accretion disk within ~ 500 yr.

Key words: galaxies: active – galaxies: nuclei

1. Introduction

One of the key questions in modern astronomy is how supermassive black holes (SMBHs) and their host galaxies coevolve (e.g., Alexander & Hickox 2012), leading to the tight correlation between the masses of SMBHs and their bulges in the present universe (e.g., Kormendy & Ho 2013). Active galactic nuclei (AGNs) are the best laboratories to understand this coevolution process, because they are in the stage where the mass accretion onto SMBHs occurs, releasing large amounts of gravitational energy as radiation (e.g., Soltan 1982; Yu & Tremaine 2002), until the SMBHs reach their achievable maximum mass limit of $M_{\text{BH}} \simeq 10^{10.5} M_{\odot}$ (Netzer 2003; McLure & Dunlop 2004; McConnell et al. 2011; Kormendy & Ho 2013; Trakhtenbrot 2014; Jun et al. 2015; Wu et al. 2015; Inayoshi & Haiman 2016; Ichikawa & Inayoshi 2017).

One of the biggest unknowns for this accretion process is how long such an AGN phase can last. Several authors indicate that the total AGN phase has a duration of 10^{7-9} yr (Marconi et al. 2004) and that one cycle of AGN should be at least over 10^5 yr, as suggested from the observations (Schawinski et al. 2015) and simulations (e.g., Novak et al. 2011). This is also consistent with the results that there are various AGN

indicators with different physical scales and that each AGN indicator has tight luminosity correlations with each other: AGN nucleus (X-ray) and the 10 pc scale AGN dusty torus (mid-infrared, hereafter MIR; Gandhi et al. 2009; Ichikawa et al. 2012; Asmus et al. 2015; Mateos et al. 2015; Ichikawa et al. 2017) and 1 kpc scale ionized gas region (so-called narrow line region or NLR; e.g., Netzer et al. 2006; Panessa et al. 2006; Berney et al. 2015; Ueda et al. 2015). This long lifetime of AGNs, however, makes it difficult for us to observe the scene where an AGN is now being quenched, or “dying,” which gives us the information on how rapidly the physics of accretion disk in an AGN is changing within the certain amount of time.

Recent observations, however, have discovered a key population of AGNs to resolve the issue above. Although they show the AGN signatures at large physical scale with ≥ 1 kpc (e.g., NLR and/or radio jets), they lack the signatures at small physical scale with < 10 pc (e.g., X-ray emission, the dust torus emission, and/or the radio core emission) or their luminosities are very faint even if they exist. They are thought to be in the transient stage where their central engine has been already fading, but the large-scale AGN indicators are still active because of the long light-crossing time (e.g., $> 10^3$ yr). They are called fading AGNs, and ~ 20 such sources have been

¹³ JSPS fellow.

reported (Schawinski et al. 2010; Schirmer et al. 2013, 2016; Schweizer et al. 2013; Ichikawa et al. 2016; Kawamuro et al. 2017; Keel et al. 2017; Sartori et al. 2018a; Villar-Martín et al. 2018; Wylezalek et al. 2018).

Among them, Arp 187 located at $z = 0.040$ ($D_L = 178$ Mpc, $1'' = 798$ pc) is one of the most promising dying AGN candidates. Dying is the final phase of a fading AGN whose current central engine is already quenched but whose large-scale AGN indicators are still alive because of the photon time delay. Ichikawa et al. (2016) used a jet lobe size discovered by the Atacama Large Millimeter/submillimeter Array (ALMA) cycle-0 observation (Ueda et al. 2014) for estimating the upper limit of the quenching time of the fading AGN. Assuming a jet angle to the line of sight of 90° and a typical expansion, the kinematic age of the radio jets is estimated to be 8×10^4 yr. Ichikawa et al. (2016) also revealed that AGN nucleus activity is already quenched with the bolometric luminosity of $L_{\text{bol}} < 10^{41}$ erg s $^{-1}$. However, Ichikawa et al. (2016) could not estimate the past AGN luminosity, and we, therefore, could not evaluate how rapidly this AGN has experienced the luminosity decline.

In this paper, we report the more multiwavelength support that Arp 187 hosts a bona fide dying AGN and that the central engine has experienced drastic luminosity decline over 10^{3-5} times within 10^4 yr, using the multiwavelength data including the newly obtained radio data with ALMA, the Karl G. Jansky Very Large Array (VLA), *Spitzer*, and NEOWISE as well as the updated analysis method to the archival 6dF optical spectrum, which has not been explored in our previous paper (Ichikawa et al. 2016). Throughout the paper, we adopt $H_0 = 70.0$ km s $^{-1}$ Mpc $^{-1}$, $\Omega_M = 0.3$, and $\Omega_\Lambda = 0.7$.

2. Analysis and Results

2.1. Radio Continuum Emission: Existence of Radio Jet Lobe

The Band 4 continuum observation of Arp 187 was performed using the ALMA 12 m array on 2016 July 25 (Cycle 3; ID = 2015.1.01005.S). We used four SPectral Windows (SPWs) with Time Domain Mode. The center frequency of the four SPWs is 133 GHz, and the total bandwidth is 8 GHz. The number of 12 m antennas was 36. The baseline lengths range from 15 m to 1124 m. Data calibration and imaging were performed using the Common Astronomy Software Applications package (CASA, ver. 4.5.3). We used the delivered calibrated uv data and made the continuum map by clipping the visibility (uv distance $\geq 10k\lambda$). The synthesized beam size is $0''.46 \times 0''.39$ (position angle (PA) = -82.7°) by adopting Briggs weighting of the visibility (robust = 0.5), and the rms noise level is 0.013 mJy beam $^{-1}$. We regard the accuracy of the absolute flux calibration as 5% throughout this article according to the ALMA Cycle 3 Technical Handbook.¹⁴

In addition, we used archival calibrated uv data obtained with VLA C- and X-bands, and made the continuum maps using CASA. We clipped the visibilities before imaging so that all the VLA and ALMA data have the same shortest UV range. The synthesized beam size of the 4.86 GHz map is $0''.43 \times 0''.34$ (PA = -4.9°) by adopting uniform weighting of the visibility, and the rms noise level is 0.28 mJy beam $^{-1}$. The synthesized beam size of the 8.44 GHz map is $0''.36 \times 0''.22$

(PA = 34.1°) by adopting Briggs weighting of the visibility (robust = 0.5), and the rms noise level is 0.20 mJy beam $^{-1}$.

The radio continuum maps are shown in Figure 1. They clearly show the structure of the jet lobes, which are located at both sides of the nucleus. The projected distance between the lobe cores is ~ 5 kpc. We estimate the kinematic age of the lobes, assuming the jet angle to the line of sight of 90° and a typical expansion speed of radio lobes (0.1c; e.g., Murgia et al. 1999; Nagai et al. 2006). This gives the kinematic age of $\sim 8 \times 10^4$ yr.

We also confirm no additional radio lobes in the field of view (FOV) of the VLA and ALMA observations. The FOV of the VLA observation at 4.86 GHz is 9.3 arcmin, which is the largest among the three observations. This corresponds to the physical size of 221 kpc in radius. If there are radio lobes outside the FOV, the lower limit of their kinematic age is 6.6×10^6 yr. Thus, Arp 187 has not launched the jet over 6.6×10^6 yr before the current 5 kpc size one, or the larger radio lobes, if any, already become undetectable because of rapid energy loss (e.g., Godfrey et al. 2017).

We also convolved these maps to $0''.47$ angular resolution to make spectral energy distributions (SEDs) of the jet lobes. The peak and total flux densities of the eastern and western lobes are summarized in Table 1. Each peak flux density is measured at the emission peak at 4.86 GHz, using the beam-matched maps. The radio SEDs of the lobes are shown in Figure 2. The spectral index α was estimated from two points at 4.86 GHz and 8.44 GHz by using a fitting function of $f_\nu \propto \nu^\alpha$. The SED shows a steep spectral index of $\alpha \approx -0.84$ for the eastern lobe (the red dashed line), and the flux point at 133 GHz is nearly on the extrapolated line from the VLA bands. This is consistent with optically thin synchrotron radiation that is expected for the jet emission. On the other hand, the flux density of the western lobes at 113 GHz is smaller than what is expected from the flux densities at 4.86 GHz and 8.44 GHz, assuming that the SED can be fitted by $f_\nu \propto \nu^\alpha$ (the black dashed line). This suggests the spectral aging for the western jet (e.g., Jamrozy et al. 2008; Saikia & Jamrozy 2009), but the exact age cannot be determined on the basis of the current SED sampling.

There is no clear emission in the nucleus (jet core) at 4.86 GHz and 8.44 GHz, although the faint emission is seen at 133 GHz. This is not due to the dynamical range limit of VLA. The 3σ upper limits of the flux densities measured in the non-beam-matched images are 0.84 mJy at 4.86 GHz and 0.60 mJy at 8.44 GHz. Assuming the spectral index of the jet core of $\alpha = -0.5$, the 133 GHz flux density is expected to be 0.16 mJy according to the upper limit of the 8.44 GHz flux density. However, the observed 133 GHz flux density is ≤ 0.052 mJy, which is three times lower than that extrapolated from the 8.44 GHz flux density. The non-detection of the continuum emission at 4.86 GHz and 8.44 GHz cannot be explained by free-free absorption, which causes the flux excess at high frequency. Thus, the non-detection at several GHz and strong constraint on the 133 GHz flux density lead to the conclusion of the presence of a significantly faint core in Arp 187.

2.2. 6dF Optical Spectra

We perform the spectral measurements to investigate the properties of the NLR. We first obtained the archival optical spectrum of Arp 187 from the 6dF galaxy survey (Jones et al. 2009). The spectrum covers a range from 3900 Å to

¹⁴ A. Remijan et al., 2015, ALMA Cycle 3 Technical Handbook Version 1.0, ALMA.

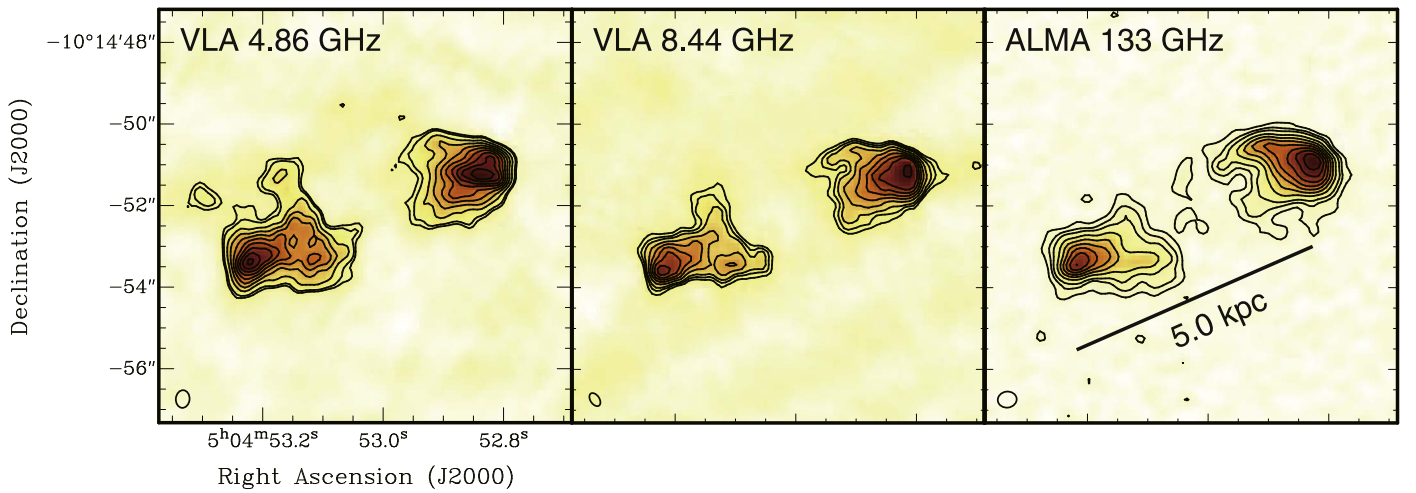


Figure 1. Radio continuum maps of Arp 187 at VLA 4.86 GHz (left), VLA 8.44 GHz (middle), and ALMA 133 GHz (right). The ellipse in the bottom-left corner shows the beam size measured in each map. The center of each panel corresponds to the peak in the *K*-band image (Rothberg & Joseph 2004). The length of each panel is $10''$, which corresponds to ~ 8 kpc. The scale in the left panel shows the separation of the two lobe cores (~ 5 kpc). The contour levels are $0.28 \text{ mJy beam}^{-1} \times (5, 6, 9, 12, 15, 18, 21, 24, 27, 30)$ for the 4.86 GHz map, $0.20 \text{ mJy beam}^{-1} \times (3, 4, 5, 7, 9, 11, 13, 15, 20)$ for the 8.44 GHz map, and $0.013 \text{ mJy beam}^{-1} \times (3, 6, 9, 15, 21, 27, 33, 39, 45, 51)$ for the 133 GHz map.

Table 1
Flux Density of the Jet Lobes

Frequency	Eastern Lobe		Western Lobe	
	Peak	Total	Peak	Total
4.86 GHz	12.0	190	13.2	160
8.44 GHz	7.53	92	9.54	100
133 GHz	0.662	5.3	0.704	7.2

Note. The unit of the flux density is mJy. These values are measured in the beam-matched images ($\theta = 0''.47$).

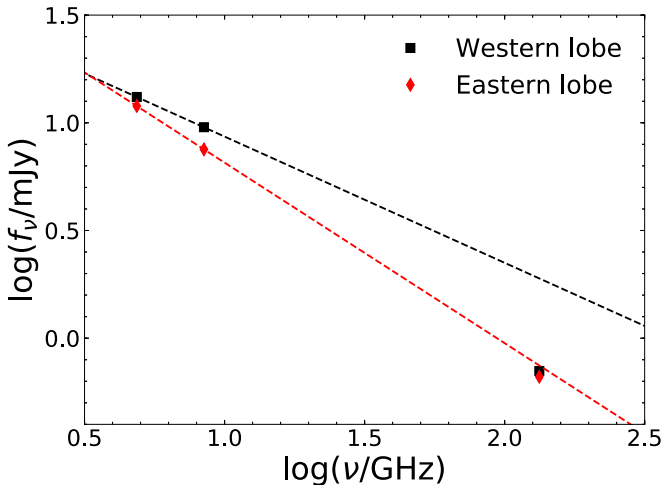


Figure 2. SEDs of the jet lobes. The spectral indexes estimated from two points at 4.86 GHz and 8.44 GHz are $\log f_\nu = 9.2 - 0.84 \log \nu$ for the eastern lobe (red) and $\log f_\nu = 6.8 - 0.59 \log \nu$ for the western lobe (black). The errors of the flux densities are smaller than the size of symbols.

7500 \AA with a fiber aperture of 6.7 arcsec (equivalent to 5.3 kpc). Because the 6dF spectra are not flux calibrated on a nightly basis, we have normalized the spectrum according to the 6dF optical photometry at the *R* band of $R = 14.33$ mag.

Figure 3 shows the optical spectrum of Arp 187 in the left panel (solid black line). The observed spectrum does not show

any features of the big blue bump originating from the AGN accretion disk or the broad emission lines (e.g., Malkan & Sargent 1982; Vanden Berk et al. 2001). Thus, we conclude that Arp 187 is at least not a type-1 AGN.

We then perform the spectral fitting to obtain the properties of the NLR. For the spectral fitting, we follow the routine in Bae et al. (2017) and later Toba et al. (2017), where they have performed the spectral fitting to the SDSS spectra. We first subtract the stellar continuum from the spectrum using a best-fit stellar template based on the wide range of the stellar population models (MILES; Sánchez-Blázquez et al. 2006) with solar metallicity and the age spanning from 60 Mys to 12.6 Gyr. To obtain the qualified stellar continuum, we mask the strong emission lines of $H\beta$, [O I], [N II], $H\alpha$, and [S II] with the masking width of 1300 km s^{-1} , which corresponds to $\text{FWHM} \sim 1000 \text{ km s}^{-1}$. We also mask the [O III] doublet with the masking width of 3000 km s^{-1} to avoid the possible contamination from the strong outflow originated from the [O III] emission lines. In addition, because some of the telluric absorptions are not well removed, we also masked those wavelength bands from the stellar spectral fitting.

From the starlight-subtracted spectrum as shown in gray line at the zero flux level in Figure 3, we then fit the $H\alpha$, $H\beta$, [N II]-doublet, [O I] $\lambda 6300$ using a single Gaussian function and [O III] doublet ([O III] $\lambda 4959, 5007$) with double-Gaussian function using the IDL/MPFIT code, which is a χ^2 -minimization routine (Markwardt 2009). We assume that the [O III] doublet and the other narrow lines have independent kinematics, whereas the [O III] doublet has the same velocity and velocity dispersion as each other. The observed spectrum (black line) and the fitting results are compiled for the entire spectral range (Figure 3, left panel) and for each line (Figure 3, right panel).

2.2.1. Existence of NLR

We first apply the emission-line diagnostics, which give a separation between the NLR ionized by AGN and the H II region in the starburst galaxies (Veilleux & Osterbrock 1987; Kewley et al. 2006). Figure 4 shows that Arp 187 is classified

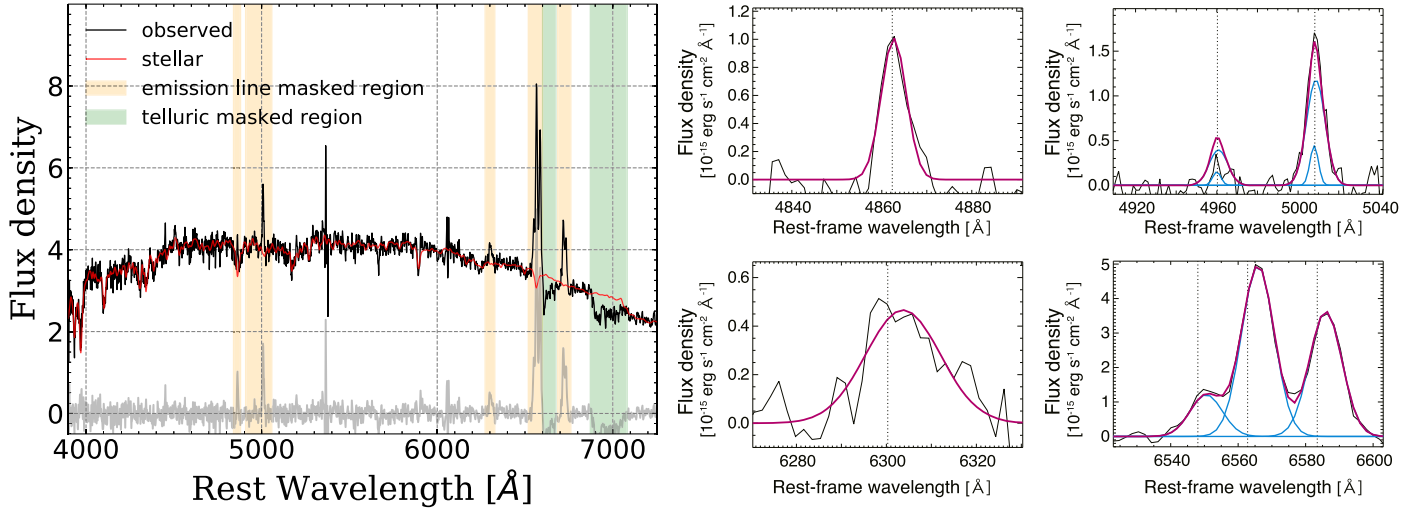


Figure 3. Left: the optical spectrum of Arp 187 (solid black line) obtained from 6dF galaxy survey. X-axis shows the rest-frame wavelength with the unit of Å. Y-axis shows the flux density with the unit of $10^{-15} \text{ erg s}^{-1} \text{ cm}^{-2} \text{ Å}^{-1}$. The best-fit stellar spectrum is also shown in the red solid line. The starlight-subtracted spectrum is shown in gray line at the zero flux level. The emission line and the telluric masked region are shown in the orange and green, respectively. Right: the spectra and the best-fit models for the Balmer lines, the [O III]-doublet ($\lambda 4959, \lambda 5007$), the [O I] $\lambda 6300$, and the [N II]-doublet lines. (upper-left: H β , upper-right: [O III] $\lambda 4959, \lambda 5007$ doublet, bottom-left: [O I] $\lambda 6300$, bottom right: H α and [N II]-doublet). The total model spectrum is shown as pink solid line. The single Gaussian line component is shown with cyan solid line (for H β , H α , and the [N II]-doublet), whereas the double-Gaussian line component is shown with two cyan lines (for the [O III] doublet) as discussed in Section 2.2.

as an AGN. Thus, it shows that Arp 187 hosts the NLR, one of the large-scale AGN indicators.

Because the diagnostic shows that [O III] $\lambda 5007$ (hereafter, [O III]) emission is dominated from the NLR, we then measure the [O III] luminosity ($L_{[\text{O III}]}$), and [O I] $\lambda 6300$ (hereafter, [O I]) luminosity ($L_{[\text{O I}]}$) to estimate the AGN bolometric luminosity because $L_{[\text{O III}]}$ alone (e.g., Heckman et al. 2004, 2005; LaMassa et al. 2013; Ueda et al. 2015) or the combination of $L_{[\text{O III}]}$ and $L_{[\text{O I}]}$ (e.g., Netzer 2009) is often used as a proxy for AGN power. The observed [O III] and [O I] luminosities are $L_{[\text{O III}]} = 6.2 \times 10^{40} \text{ erg s}^{-1}$ and $L_{[\text{O I}]} = 3.8 \times 10^{40} \text{ erg s}^{-1}$. We also calculate an extinction-corrected, intrinsic luminosity of [O III] ($L_{[\text{O III}]}^{\text{int}}$) and [O I] ($L_{[\text{O I}]}^{\text{int}}$) luminosities from the Balmer decrement of H α /H β (e.g., Calzetti et al. 1994; Domínguez et al. 2013). The values are $L_{[\text{O III}]}^{\text{int}} = 3.2 \times 10^{42} \text{ erg s}^{-1}$ and $L_{[\text{O I}]}^{\text{int}} = 2.0 \times 10^{42} \text{ erg s}^{-1}$. We calculate the AGN bolometric luminosity L_{bol} using the both lines (Netzer 2009; Matsuoka & Woo 2015) by

$$\log L_{\text{bol}} = 3.8 + 0.25 \log L_{[\text{O III}]}^{\text{int}} + 0.75 L_{[\text{O I}]}^{\text{int}}. \quad (1)$$

The estimated value is $\log(L_{\text{bol}}/\text{erg s}^{-1}) = 46.2$, which reaches to the typical luminosity of the SDSS quasars at $z \sim 1-2$ (e.g., Shen et al. 2011).

2.2.2. NLR Size

The size of the NLR is also an important indicator to estimate the fading timescale of AGN for Arp 187. Because the integral field unit (IFU) observations are still not available, we estimate the NLR size from the empirical relationship between the [O III] emission size and the [O III] luminosity.

The [O III] emission sizes have been measured from either narrowband imaging (Bennert et al. 2002; Schmitt et al. 2003), long-slit spectroscopy (Fraquelli et al. 2003; Bennert et al. 2006; Greene et al. 2011; Hainline et al. 2013), or the IFU observations (Humphrey et al. 2010; Husemann et al. 2013;

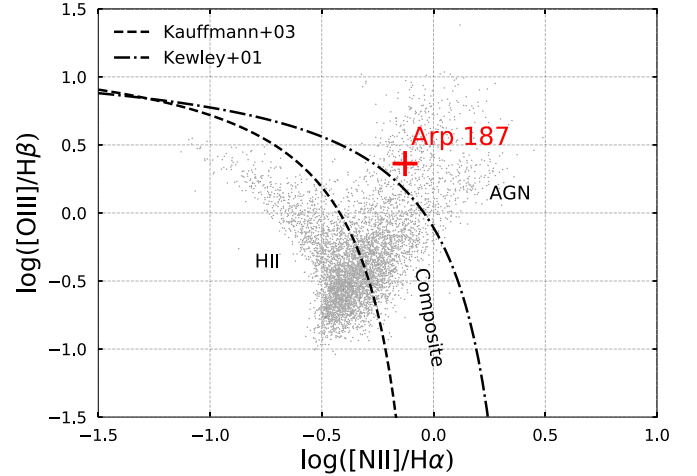


Figure 4. Classification of the galaxies into AGN, composite galaxies, and H II regions using line diagnostics diagrams (Kewley et al. 2001, 2006). The dotted-dashed/dashed line represents the relation of Kewley et al. (2001)/Kauffmann et al. (2003), respectively. Arp 187 is located in the locus of AGN (red cross). Gray dots represent the data points of SDSS DR7 galaxies (Abazajian et al. 2009).

Liu et al. 2013; Karouzos et al. 2016; Bae et al. 2017). The narrowband imaging is more often used for studying the NLR morphology, whereas the long-slit spectroscopy and IFU have an advantage to reach shallower sensitivity limits.

We first estimate the NLR sizes (R_{NLR}) using the size–luminosity relations of Bae et al. (2017) obtained from the IFU observations of nearby type-2 Seyferts and quasars. This relation has two advantages; (1) their study uses the extinction-uncorrected [O III] luminosity for the size–luminosity relation to reduce the uncertainty of the extinction correction to estimate the intrinsic [O III] luminosity, and (2) they estimate the NLR size on the basis of the line diagnostic diagrams discussed in Section 2.2, which pick up the region where the [O III] emission is dominated from AGN. The size–luminosity

relation of Bae et al. (2017) is given by

$$\log\left(\frac{R_{\text{NLR}}}{\text{pc}}\right) = 0.41 \times \log\left(\frac{L_{[\text{O III}]}}{\text{erg s}^{-1}}\right) - 14.00. \quad (2)$$

The estimated NLR size is $R_{\text{NLR}} \simeq 530$ pc.

We also estimate the [O III] emitting sizes ($R_{[\text{O III}]}$) using the size–luminosity relations from the literature. Note that the relation is based on the [O III] emission size; therefore, the estimated size should be the upper bound of the NLR size because the NLR should fulfill the certain emission-line ratios as shown in Figure 3. We apply the relation according to the narrowband imaging observations of the quasar population (Schmitt et al. 2003) by

$$\log\left(\frac{R_{[\text{O III}]}}{\text{pc}}\right) = 0.42 \times \log\left(\frac{L_{[\text{O III}]}}{\text{erg s}^{-1}}\right) - 14.72. \quad (3)$$

This gives $R_{\text{NLR}} < R_{[\text{O III}]} \simeq 1.4$ kpc, which is ~ 2.5 times larger than R_{NLR} obtained above. This result is in good agreement with the previous IFU studies (Karouzos et al. 2016; Bae et al. 2017), who reported that $R_{[\text{O III}]}$ is on average a few times larger than R_{NLR} . In this study, we assume $R_{\text{NLR}} = 530$ –1400 pc as the possible NLR size range.

2.3. Spitzer/IRS Spectra

Because the detailed spectral analysis of Arp 187 obtained from the *Spitzer*/InfraRed Spectrograph (IRS) is compiled in Ichikawa et al. (2016), here we provide a brief summary of the findings. We have found that the thermal emission from the AGN is already weak in Arp 187, with an upper bound of the $12 \mu\text{m}$ luminosity of $L_{12\mu\text{m}} < 1.5 \times 10^{42}$ erg s $^{-1}$. This is equivalent to $L_{\text{bol}} < 2.2 \times 10^{43}$ erg s $^{-1}$ using the relation of $L_{12\mu\text{m}}$ and 14–195 keV luminosities (Ichikawa et al. 2017) and the bolometric correction of $L_{\text{bol}}/L_{14-195} = 8.47$ (Ricci et al. 2017b; Ichikawa et al. 2019). The spectrum of Arp 187 shows a marginal detection of the [O IV] 25.89 μm line at $S/N \sim 3$, which is also a widely used AGN indicator. The [O IV] luminosity is obtained with $L_{[\text{O IV}]} = 6.7 \times 10^{40}$ erg s $^{-1}$, which is equivalent to $L_{2-10} = 3.0 \times 10^{43}$ erg s $^{-1}$ according to the luminosity relations obtained by LaMassa et al. (2010). Because the ionization potential of [O IV] is higher ($E_p = 54.9$ eV) than other typical NLR indicators, including [O III] line (e.g., Rigby et al. 2009), the emission size is expected to be smaller than that of [O III] (Komossa et al. 2008; Toba et al. 2017), which is 0.5–1.4 kpc in this study. Thus, we take the emission size of < 1.4 kpc as a fiducial value.

2.4. WISE Colors

IR color–color selection is useful to identify AGN candidates using the feature of the MIR bump originated from the AGN torus. Figure 5 shows the location of Arp 187 on the *WISE* color–color plane. It is known that increasing levels of AGN contribution to the MIR emission moves sources upward in the color–color plane with the color cut of $W1 - W2 > 0.8$ (orange area; Stern et al. 2012) and also within the AGN wedge (blue area; Mateos et al. 2012). The figure clearly shows that Arp 187 does not fulfill either of the criteria above, indicating either (1) Arp 187 does not host AGN or (2) the AGN activity is quite weak even if it exists (on average $L_{14-195} < 10^{43}$ erg s $^{-1}$, as suggested by Ichikawa et al. 2017).

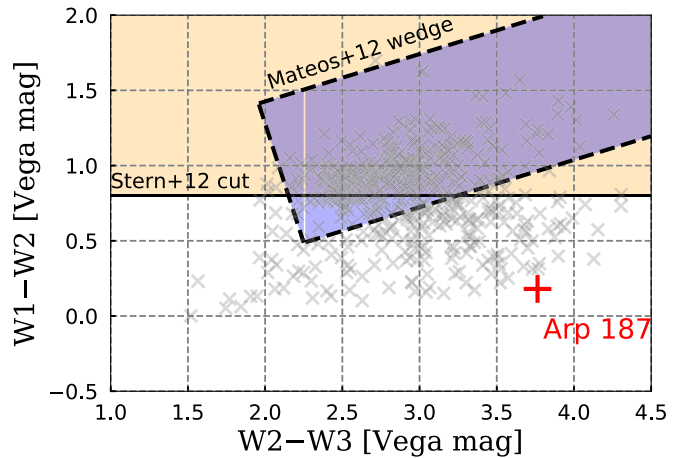


Figure 5. *WISE* W1 (3.4 μm)–W2 (4.6 μm) vs. W2 (4.6 μm)–W3 (12 μm) two color diagram in the unit of Vega magnitude. The gray cross represents the *Swift*/BAT AGN sample in the local universe. The orange and purple area represents the AGN region proposed by Stern et al. (2012) and Mateos et al. (2012), respectively.

2.5. WISE IR Time Variability

It is worthwhile to trace the IR luminosity drop from the AGN torus after the AGN quenching. Because Arp 187 is bright enough to be detected in the single exposure with the *WISE* mission, we have collected both cryogenic (*WISE* All sky database) and postcryogenic multiepoch photometry (*WISE* 3 band and Post-Cryo database) from the ALLWISE (Wright et al. 2010; Mainzer et al. 2011) covering the observation between 2010 January and 2011 February (MJD–55000 = 200–600), and the most recent NEOWISE (Mainzer et al. 2014) data release 2018 covering the observation between 2013 December 13 and 2017 December 13, UTC (MJD–55000 = 1600–3100). *WISE* has a 90 minute orbit and conducts ≈ 12 observations of a source over a ≈ 1 day period, and a given location is observed every 6 months.

In this study, we used standard aperture magnitude ($w1/2\text{mag}$). We applied a cross-matching radius of 2 arcsec, according to the positional accuracy with the 2MASS catalog (see also Ichikawa et al. 2012, 2017). After this matching, 26 and 122 data points were obtained from the ALLWISE and NEOWISE epoch, respectively. Then we select good quality single-epoch data points according to the good quality frame score ($\text{qual_frame} > 0$ and $\text{qi_fact} > 0$), locating them with enough distance from the South Atlantic Anomalies ($\text{saa_sep} > 0$), and avoiding the possible contamination from the moon ($\text{moon_masked} = 0$). This reduces the sample into 24 (ALLWISE) and 109 (NEOWISE), respectively. Finally, we applied the aperture measurement quality flag ($w1/2\text{flg} = 0$) in order to avoid the contamination in the aperture. The final data points are 10 (W1) and 8 (W2) for ALLWISE 43 (W1) and 21 (W2) for NEOWISE. All the data points fulfill the flux quality $\text{ph_qual} = \text{A}$, with a signal-to-noise ratio larger than 10.0. We also checked sources of contamination and/or biased flux due to proximity to an image artifact (e.g., diffraction spikes, scattered-light halos, and/or optical ghosts), using the contamination flag cc_flags . All the data points are $\text{cc_flags} = 0$, that are unaffected by known artifacts.

Figure 6 shows the light curve of W1 (3.4 μm) and W2 (4.6 μm). The light curves in the W1 and W2 span a baseline of roughly 2800 days $\simeq 7.7$ yr. Each observation is shown in blue, and binned observations within 1 day are also shown in orange.

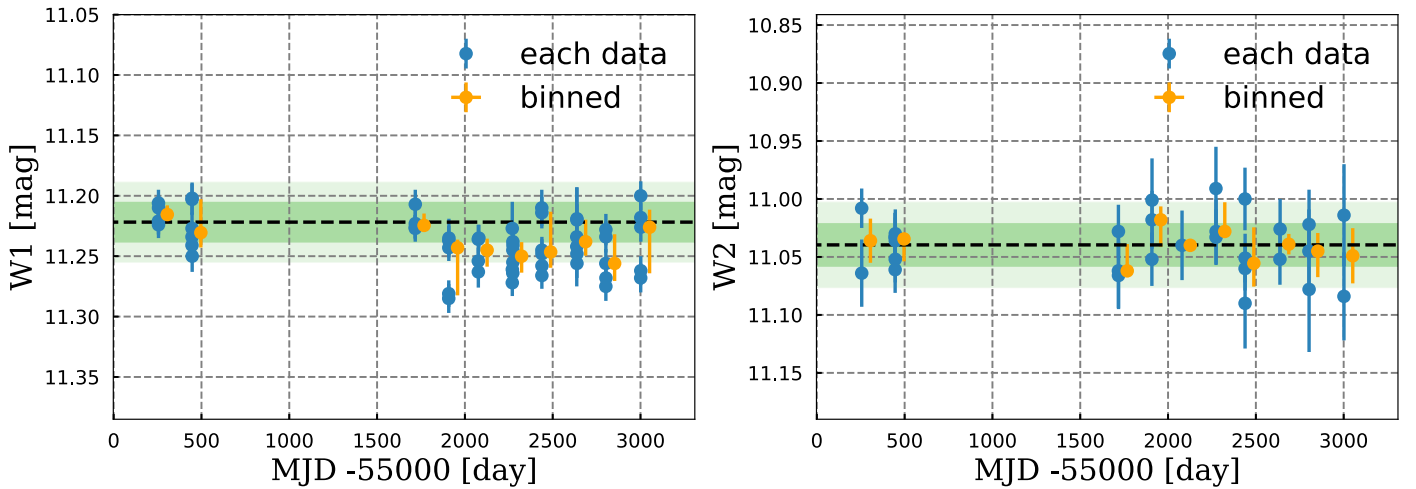


Figure 6. Infrared light curves of Arp 187 in the W1 and W2 band. The single exposures with the error are shown in blue, and the median value in each epoch is shown in orange circle with the error bars showing the interpercentage range with 68% of the sample. The orange circles are shifted to 50 days after the real values for clarity. The dashed line with green shade is the flux obtained from ALLWISE with the 1σ (dark green) and 2σ (light green) scatter, representing the average magnitude in the ALLWISE epoch.

As shown in Figure 6, no clear variability is detected in the ALLWISE and NEOWISE epoch, and also between the two epochs. Actually, the ALLWISE catalog provides a variability flag (`var_flag`) and its value is `var_flag` = 0, suggesting that the significant variability between different exposures are not detected during the ALLWISE survey, which shows the consistent result.

2.6. Relationship between $12\ \mu\text{m}$ and [O III] Luminosities

It is widely known that both $12\ \mu\text{m}$ and the [O III] luminosities are good proxies for AGN power, and it is a natural consequence that there is a luminosity correlations between $12\ \mu\text{m}$ and the [O III] luminosities (e.g., Toba et al. 2014).

Figure 7 shows the relationship between $12\ \mu\text{m}$ and [O III] $\lambda 5007$ luminosities using the SDSS DR12 type-2 AGN sample with the cross-matching by the WISE W3 ($12\ \mu\text{m}$) band. As expected, the two AGN indicators have a nice luminosity correlation. However, Arp 187 does not follow the luminosity relation and is located at the right bottom in the plane, suggesting that Arp 187 is in the locus of a dying AGN. Ichikawa & Tazaki (2017) estimated the typical cooling timescale of the dusty torus once the AGN is suddenly quenched. The thermal MIR dust emission from AGN should decay times of 10–100 yr, mainly depending on the time-lag caused by the light-travel time from the nucleus to the dust sublimation radius, whereas the $L_{[\text{O III}]}$ remains the same luminosity for over $>10^3$ yr because of its larger physical size. Ichikawa & Tazaki (2017) also calculated how those dying AGNs move in the luminosity–luminosity plane of the two AGN indicators, and showed that those dying AGNs should locate at the bottom right of the luminosity relation. The location of Arp 187 in Figure 7 is consistent with the idea, and below the relationship of the line after 30 yr of AGN quenching (the orange dashed line).

2.7. X-Ray Observations

Although the X-ray observations give us the current AGN activity without the concern of the obscuration up to $\log N_{\text{H}} \simeq 24$ (e.g., Ricci et al. 2015, 2017a), we have not

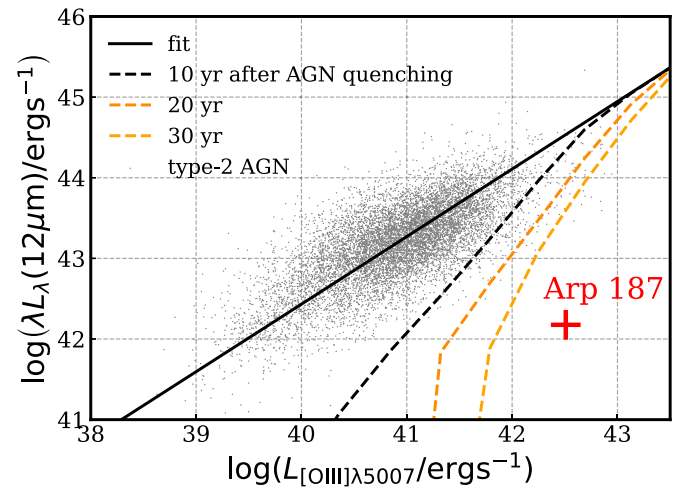


Figure 7. Correlation between the [O III] $\lambda 5007$ and $12\ \mu\text{m}$ luminosities. The black solid line represents the regression line obtained from the bisector fitting of the type-2 AGN sample from SDSS DR12 galaxies (gray dots). The dashed lines represent the time evolution of the AGN luminosity relation the [O III] $\lambda 5007$ and $12\ \mu\text{m}$ after AGN quenching (Ichikawa & Tazaki 2017); 10 yr (black), 20 yr (dark-orange), and 30 yr (orange). The location of Arp 187 is shown with a red cross.

found any previous X-ray observations for Arp 187, and therefore only the upper bounds obtained from the available all sky X-ray surveys.

Arp 187 is not in the catalog of *Swift*/BAT 105 month all sky survey with the limiting flux at the 14–195 keV band of $f_{14-195}^{(\text{lim})} = 8.0 \times 10^{-12} \text{ erg s}^{-1} \text{ cm}^{-2}$ (Oh et al. 2018). This gives a very shallow upper bound of $L_{14-195} < 2.8 \times 10^{43} \text{ erg s}^{-1}$, which is equivalent to $L_{\text{bol}} < 2.4 \times 10^{44} \text{ erg s}^{-1}$ under the assumption of $L_{\text{bol}}/L_{14-195} = 8.47$ (Ricci et al. 2017b).

The *ROSAT* All Sky Survey also shows non-detection at the energy range of 0.5–2.0 keV ($f_{\text{lim}} = 2.5 \times 10^{-12} \text{ erg s}^{-1} \text{ cm}^{-2}$; Voges et al. 1999). This also gives a shallow upper bound of $L_{0.5-2} < 8.8 \times 10^{42} \text{ erg s}^{-1}$, which is equivalent to $L_{\text{bol}} < 2.8 \times 10^{44} \text{ erg s}^{-1}$ using $L_{2-10}/L_{0.5-2} = 1.57$ under the assumption of the photon index $\Gamma = 1.8$ (Ricci et al. 2017a) and $L_{\text{bol}}/L_{2-10} = 20$ (Ricci et al. 2017b).

Table 2
AGN Indicators and Their Estimated Luminosities

Large-scale AGN Indicators (>100 pc)							
Type of AGN Indicators	AGN Sign	$\log(L_{\text{AGN}}/\text{erg s}^{-1})$	$\log(L_{\text{bol}}/\text{erg s}^{-1})$	$\log \lambda_{\text{Edd}}$	Size (radius)	$t_{\text{retro}}^{\text{a}}$	References
jet lobe	✓	2.5 kpc	8.1×10^4 yr	Section 2.1
NLR ([O III] λ 5007)	✓	$\log L_{[\text{O III}]}^{\text{int}} = 42.51$	46.15	-0.77	0.5–1.4 kpc	$(1.7\text{--}4.6) \times 10^3$ yr	Section 2.2
NLR ([O IV] λ 25.89 μm)	✓	$\log L_{[\text{O IV}]}^{\text{int}} = 40.83$	44.78	-2.15	≤ 1.4 kpc	$\leq 4.6 \times 10^3$ yr	Section 2.3
Small-scale AGN Indicators (<10 pc)							
Dust torus (<i>Spitzer</i> /IRS Spec)	X	$\log L_{12\ \mu\text{m}} < 42.18$	$< 43.34^{\text{a}}$	< -3.59	$\simeq 10$ pc	10–100 yr	Section 2.3
Dust torus (<i>WISE</i> IR colors)	X	10–100 yr	Section 2.4
Dust torus (<i>WISE</i> IR light curve)	X	10–100 yr	Section 2.5
Dust torus ($L_{[\text{O III}]}$ versus $L_{12\ \mu\text{m}}$)	X	$\log L_{12\ \mu\text{m}} < 42.18$	$< 43.34^{\text{a}}$	< -3.59	$\simeq 10$ pc	>30 yr	Section 2.6
jet core	X	$\log L_{5\text{GHz}} < 37.57$	≤ 1 pc	Current	Section 2.1
BLR (optical Spec)	X	< 0.1 pc	Current (1–10 yr)	Section 2.2
Electron corona (X-ray)	X	$\log L_{2-10} < 43.44$	$< 44.38^{\text{a}}$	< -2.55	$\ll 0.1$ pc	Current	Section 2.7
Other Relations							
BH fundamental plane (FP)	...	$\log L_{2-10} < 39.60$	$< 40.90^{\text{a}}$	< -6.03	...	Current	Section 2.8

Note. The list of AGN indicators and the retrospective time (t_{retro}) of the AGN indicator. Except for the jet lobe, the all time is the light-crossing time with the definition of $t_{\text{lc}} = \text{size}/c$.

^a From the X-ray luminosities, we use the bolometric correction of $L_{\text{bol}}/L_{2-10} = 20$ (Ricci et al. 2017b). Then, under the assumption of the photon index of $\Gamma = 1.8$ (Ricci et al. 2017a), we use the conversion among the X-ray luminosities of $L_{2-10}/L_{14-195} = 0.42$ and $L_{2-10}/L_{0.5-2} = 1.57$. We also use the luminosity relations between $L_{12\ \mu\text{m}}$ and L_{14-195} of $\log(L_{12\ \mu\text{m}}/10^{43} \text{ erg s}^{-1}) = -0.21 + 1.05 \log(L_{14-195}/10^{43} \text{ erg s}^{-1})$ to estimate the bolometric luminosity from $L_{12\ \mu\text{m}}$ (Ichikawa et al. 2017). For the estimates of the Eddington luminosity ratio $\lambda_{\text{Edd}} = L_{\text{bol}}/L_{\text{Edd}}$, we apply the black hole mass of $M_{\text{BH}} = 6.7 \times 10^8 M_{\odot}$, which leads to $L_{\text{Edd}} = 8.4 \times 10^{46} \text{ erg s}^{-1}$.

Other X-ray catalogs, such as the third *XMM-Newton* serendipitous source catalog (3XMM-DR7; Rosen et al. 2016) and the Chandra Source Catalog (CSC Release 2.0; Evans et al. 2010), do not contain the observations of Arp 187.

2.8. Black Hole Fundamental Plane

The fundamental plane of the black hole gives a relationship among three physical quantities of L_{2-10} , core $L_{5\text{GHz}}$, and the black hole mass M_{BH} (e.g., Merloni et al. 2003; Falcke et al. 2004; Yuan & Narayan 2014). Ichikawa et al. (2016) discussed that once the upper bound of $L_{5\text{GHz}}$ is given, we can estimate the upper bound of L_{2-10} , because the black hole mass in Arp 187 is estimated to be $M_{\text{BH}} = 6.7 \times 10^8 M_{\odot}$. The upper bound of $L_{5\text{GHz}} \leq 3.7 \times 10^{37} \text{ erg s}^{-1}$ obtained by the VLA observation gives $L_{2-10} \leq 4.0 \times 10^{39} \text{ erg s}^{-1}$ using the relation of Yuan & Cui (2005). This is equivalent to $L_{\text{bol}} \leq 8.0 \times 10^{40} \text{ erg s}^{-1}$, indicating that the central engine is already quenched.

3. Discussion

3.1. AGN Indicators and Scenarios of Current AGN Activity

Our multiwavelength measurements of the AGN indicators show that we have successfully found the large-scale (>100 pc) AGN indicators but not the indicators for the small-scale ones with ≤ 10 pc. Table 2 summarizes the AGN indicators for Arp 187.

There are two possible scenarios that can account for these seemingly contradictory results between the larger (>100 pc) and smaller (≤ 10 pc) scales. One is that the AGN activity still exists but the emission is highly obscured along the line of sight, while being unobscured toward the jet and/or the NLR direction (e.g., Sartori et al. 2018a). The other is that the AGN

activity in Arp 187 has already been quenched, whereas the NLRs still remain bright because of the light-travel time from the central engine. The first scenario is unlikely for Arp 187 for two reasons. One is the absence of the AGN torus emission in the *Spitzer*/IRS spectra, as well as the other torus indicators obtained from *WISE*. If the central engine is highly obscured, then most of the emission is absorbed by the dust, and then it re-emits and produces the bump in the MIR (e.g., Ichikawa et al. 2014), which we could not find. Another point is the absence of the jet core, which is irrelevant to the concern of absorption and its existence is the ubiquitous trend for AGN (Blandford & Königl 1979; Hada et al. 2011), although there are some rare exceptions (Cordey 1987; Dwarakanath & Kale 2009). Thus, our results prefer the scenario of a dying AGN.

One might argue that the absence of the big blue bump and the broad emission-line region (BLR) is due to the absorption by the dusty torus (e.g., Antonucci 1993; Nagar et al. 2002). It is true in general, but because the torus emission is already weak for Arp 187, as discussed in Section 2.3, the most plausible explanation is that the central engine including the accretion disk and the BLR becomes already very faint or might be diminished.

The disappearing timescale of the BLR is poorly known at present. One possible implication of this comes from the observations of changing-look AGNs, which show the AGN type change in a human timescale (e.g., Tohline & Osterbrock 1976; Antonucci & Cohen 1983; Alloin et al. 1985; LaMassa et al. 2015; MacLeod et al. 2016; Ruan et al. 2016; Yang et al. 2018). One of the findings of the ~ 10 yr long monitoring of changing-look AGNs is that the BLR can disappear within a few years, whereas the physical mechanism of the disappearance is still under debate (Lawrence 2018). Thus, in this paper we compile the timescale of BLR as 1–10 yr in Table 2.

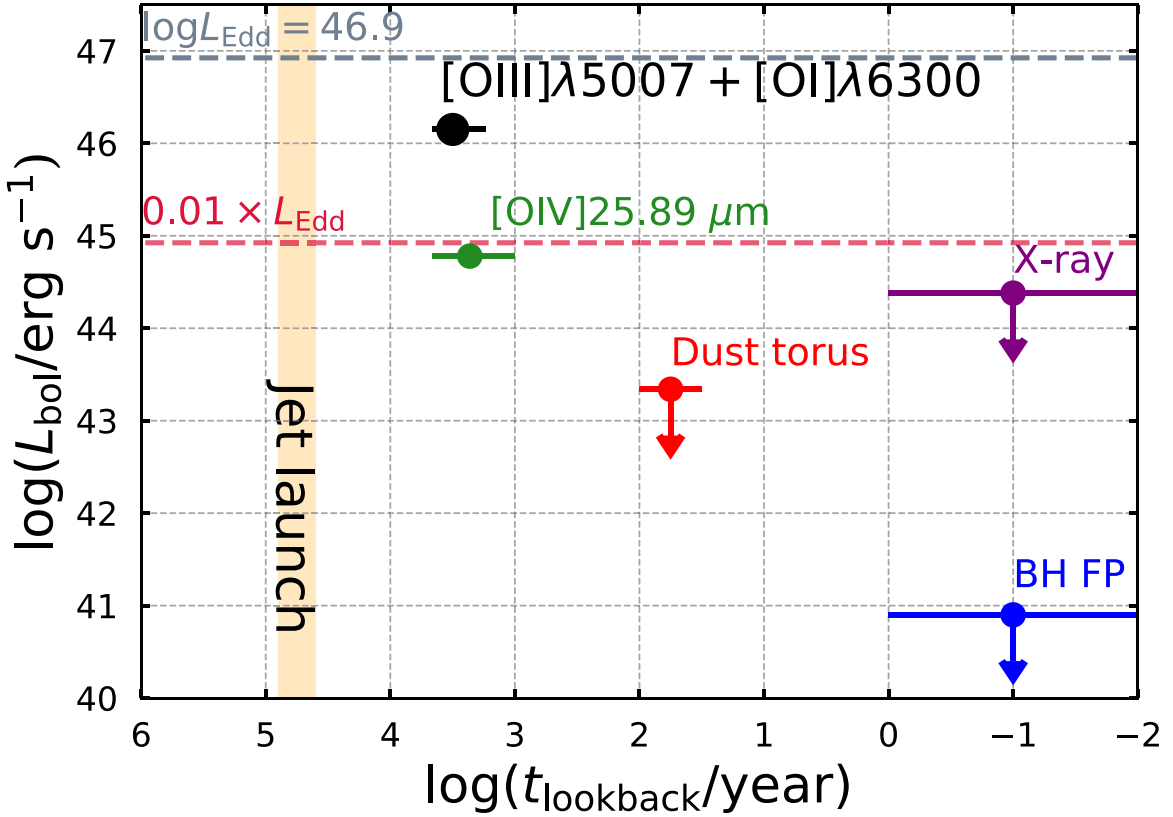


Figure 8. Long-term light curve of Arp 187 based on the AGN indicators with multiple physical scales. See Table 2 for the details of the each AGN indicator.

3.2. Luminosity Decline and Corresponding Timescales

One of our goals is to constrain how rapidly the AGN has faded in Arp 187. We summarize the long-term luminosity decline of Arp 187 in Figure 8. This figure shows that the AGN has experienced the drastic luminosity decline by the factor of 10^{3-5} times within $\simeq 10^4$ yr.

One question arises as to how to describe the sudden quenching of AGN within $\simeq 10^4$ yr and how this timescale is connected to the physical properties of the accretion disk of AGN. We here consider three possible timescales: the orbital, thermal, and the viscous (inflow) timescales, by following the discussions of Czerny (2006) and Stern et al. (2018). If the accretion flow is roughly Keplerian, the dynamical timescale of the accretion disk is given by $t_{\text{dyn}} \sim 1/\Omega_K$, where Ω_K is the Keplerian orbital angular frequency. The thermal timescale, which is corresponding to the disk cooling, is given by $t_{\text{th}} \sim 1/\alpha \Omega_K$, where α is the viscosity parameter (Shakura & Sunyaev 1973; Kato et al. 2008). The viscous timescale is also given by $t_{\text{vis}} \sim (h/R)^{-2} t_{\text{th}}$, where h/R is the disk aspect ratio. The numerical simulations derive the estimation of $\alpha \sim 0.03$ (Hirose et al. 2009; Davis et al. 2010); therefore, we use $\alpha_{0.03} = \alpha/0.03$ as the fiducial value. The disk aspect ratio is typically very small, and we assume $h/R \sim 0.05$ by following Stern et al. (2018).

We first determine the boundary accretion disk radius R , within which it emits the UV radiation, where UV represents the wavelength of $\lambda < 3500 \text{ \AA}$, and the typical wavelength range of the big blue bump (e.g., Malkan & Sargent 1982; Vanden Berk et al. 2001). Using the obtained parameter for Arp 187, the BH is estimated to be $M_{\text{BH}} = 6.7 \times 10^8 M_{\odot}$ and the maximum Eddington ratio in this study is $\lambda_{\text{Edd}} = 0.17$ obtained from the NLR. The gravitational radius is given by

$R_g = 2GM_{\text{BH}}/c^2 \sim 13 \text{ au}$. The AGN bolometric luminosity is governed by $L_{\text{bol}} = \eta \dot{M} c^2$, where η is the radiation efficiency. The typical value is estimated as $\eta \sim 0.1$ (Soltan 1982). The mass accretion rate \dot{M} is therefore given by

$$\dot{M} \approx 2.8 M_{\odot} \text{yr}^{-1} \eta_{0.1}^{-1} M_{\text{BH},0} \lambda_{\text{Edd},0.17}. \quad (4)$$

Here, $\eta_{0.1} = \eta/0.1$, $M_{\text{BH},0} = M_{\text{BH}}/6.7 \times 10^8 M_{\odot}$, and $\lambda_{\text{Edd},0.17} = \lambda_{\text{Edd}}/0.17$.

Assuming a standard thin-disk AGN model, the disk radius R is linked to the disk temperature T in Equation of (3.57) of Kato et al. (2008) written by

$$R = \frac{3GM\dot{M}}{8\pi\sigma T^4}, \quad (5)$$

where σ is a Stefan–Boltzmann constant. Combining Equation (5) and (4) with Wien’s law ($(\lambda/\text{\AA}) = 2.9 \times 10^7/T$), the typical radius R can be given by

$$\frac{R}{R_g} = 100 \eta_{0.1}^{-1/3} M_{\text{BH},0}^{-1/3} \lambda_{\text{Edd},0.17}^{1/3} \lambda_{3500}^{4/3}, \quad (6)$$

where $\lambda_{3500} = \lambda/3500 \text{ \AA}$. Thus we apply $R_{100} = R/100R_g$ as a fiducial value for the UV-emitting disk size.

We can then parameterize the disk timescales as

$$t_{\text{dyn}} \sim 100 \text{ day} \times M_{\text{BH},0} R_{100}^{3/2}, \quad (7)$$

$$t_{\text{th}} \sim 10 \text{ yr} \times \alpha_{0.03}^{-1} M_{\text{BH},0} R_{100}^{3/2}, \quad (8)$$

$$t_{\text{vis}} \sim 1.6 \times 10^4 \text{ yr} \times \left(\frac{h/R}{0.05}\right)^{-2} \alpha_{0.03}^{-1} M_{\text{BH},0} R_{100}^{3/2}. \quad (9)$$

Because Arp 187 has not shown the big blue bump and the torus emission (whose source of nutrition is the UV photons)

Table 3
Observational Properties of Dying AGN, Fading AGN, and Changing-look Quasars

	Dying AGN (Arp 187)	Fading AGN	Changing-look Quasar
Definition	AGN whose current (small-scale) AGN signature is dead, but past AGN signature is still alive	AGN with weaker current L_{AGN} compared to that of past AGN signatures	Quasars with broad Balmer line (dis)appearance associated with continuum change by a factor of ~ 10
Small-scale (< 10 pc) AGN signs	Dead	Alive (but weak)	Alive
Large-scale (> 100 pc) AGN signs	Alive	Alive	Alive
Jet core features	No	Yes (?) ^(B1)	...
Jet lobe features	Yes
$\Delta L_{\text{AGN}}^{(a)}$	10^{3-5}	10^{1-4}	~ 10
$\Delta t^{(b)}$	$\leq 10^4$ yr	10^{4-5} yr (using EELR ⁽⁺⁾)	$\sim 1-10$ yr ^(C1,C3,C4,C6)
L_{AGN} (current)	$< 10^{42}$ erg s ⁻¹	10^{43-45} erg s ⁻¹	$> 10^{43}$ erg s ⁻¹
L_{AGN} (before fading)	$\sim 10^{46}$ erg s ⁻¹	10^{44-46} erg s ⁻¹	$> 10^{44}$ erg s ⁻¹
Redshift (z)	0.04	0.01–0.3 ^(B5, B10)	0.01–1.0 ^(C1,C3,C4,C6)
Origin of variability	Viscous	Viscous	Unknown (thermal? ^(C8-C10) or Magnetically elevated disk? ^(C7))
Host galaxies	Merger remnant	Merger system/remnants (?) ^(B5)	...
Number of sources found	...	~ 20 sources ^(B1-B13)	> 40 sources ^(C1-C6)
Most known object names	Arp 187 ^(A1) (NGC 7252? ^(A2))	IC 2497 (Hanny’s Voorwerp) ^(B1-B8) Teacup galaxy ^(B5,B6,B12) , etc.	SDSS J0159+0033 ^(C1) SDSS J1011+5442 ^(C2) , etc.

Note. (1) EELR stands for extended AGN photoionized emission-line region with the physical scale of ~ 10 kpc. (a) Observed or inferred AGN luminosity decline. (b) The timescale of the AGN luminosity decline of ΔL_{AGN} . “...” in the column represents that there are no clear observations or consensus from the literature.

References. dying AGN: (A1) Ichikawa et al. (2016), (A2) Schweizer et al. (2013); fading AGN: (B1) Józsa et al. (2009), (B2) Lintott et al. (2009), (B3) Schawinski et al. (2010), (B4–B6) Keel et al. (2012, 2015, 2017), (B7, B8) Sartori et al. (2018a, 2018b), (B9, B10) Schirmer et al. (2013, 2016), (B11) Kawamuro et al. (2017), (B12) Villar-Martín et al. (2018), (B13) Wylezalek et al. (2018); changing-look quasar: (C1) LaMassa et al. (2015), (C2) Runnoe et al. (2016), (C3) Ruan et al. (2016), (C4) MacLeod et al. (2016), (C5) Gezari et al. (2017), (C6) Yang et al. (2018), (C7) Dexter & Begelman (2019), (C8) Noda & Done (2018), (C9) Ross et al. (2018), (C10) Stern et al. (2018).

for at least the last 10 yr (see also Figure 8), the dynamical and thermal timescales are unlikely and too short to be happening. On the other hand, the viscous timescale seems to be a little longer compared to the quenching timescale of $< 10^4$ yr. However, because the NLR traces higher energy UV photons with > 10 eV, the corresponding disk region becomes more inner with $R \lesssim 10 R_g$, whose viscous timescale is $\lesssim 500$ yr. This is consistent with our strongest upper bound of ~ 3000 yr (see Table 2). Thus, our rough estimation suggests that the viscous timescale most closely matches the observed quenching timescale.

3.3. Comparison between Dying AGN and Fading AGN

The absence of small-scale AGN signatures and the timescale discussed in Section 3.2 support that Arp 187 has been in a later fading phase, or dying phase, compared to other fading AGNs because the UV-emitting region in Arp 187 likely disappeared, and the large-scale AGN indicators are observable as remnant signs of an AGN. On the other hand, the previously reported fading AGNs are considered to be earlier fading stage because they still host clear UV, MIR, or X-ray emission in the core, suggesting that the UV-emitting region is still alive (e.g., Keel et al. 2015, 2017; Sartori et al. 2018a). We have summarized the comparison of properties of our dying AGN and fading AGN in Table 3.

One important question is how many such dying AGNs have been already reported in the population of fading AGNs from

the literature. Although most fading AGNs still show MIR or X-ray emission in the core, one fading AGN in NGC 7252 might fulfill dying the AGN criterion. Schweizer et al. (2013) showed that NGC 7252 hosts large [O III] $\lambda 5007$ bright nebulae that belong to a stream of tidal-tail gas falling back to the host galaxy. The bright [O III] nebulae require the AGN luminosity larger than $L_{\text{bol}} > 5 \times 10^{42}$ erg s⁻¹, whereas the current X-ray upper bound gives $L_{\text{bol}} < 5 \times 10^{40}$ erg s⁻¹. Considering the nebulae distance, NGC 7252 might have experienced a luminosity decline by two orders of magnitude over the past 10^{4-5} yr, and the current AGN activity is well below $L_{\text{bol}} < 10^{42}$ erg s⁻¹, suggesting that the central engine is already dead.

Note that the past inferred AGN luminosity is completely different between Arp 187 and NGC 7252. Arp 187 reached a quasar-like luminosity with $L_{\text{bol}} > 10^{46}$ erg s⁻¹, whereas that of NGC 7252 is well below the quasar level or, more likely, Seyfert level luminosity with $L_{\text{bol}} > 5 \times 10^{42}$ erg s⁻¹. Schweizer et al. (2013) also reported that the central gas disk of NGC 7252 contains the large amount of molecular gas with $> 10^9 M_\odot$, suggesting that the AGN feedback activity has failed to remove the gas in the host galaxy. Therefore, the gas content difference between NGC 7252 and Arp 187 would be a good testbed to investigate the effect of AGN feedback because these two galaxies have already experienced the one cycle of AGN activity for at least 10^5 yr (Schawinski et al. 2015) but with different AGN luminosity.

3.4. Comparison of the Causes of Luminosity Changes between Dying AGNs and Changing-look Quasars

It is worthwhile to note the difference of the accretion mechanism between our dying AGN in Arp 187 and a recently discovered class of “changing-look quasars,” in which the strong UV bump and broad emission lines associated with optically bright quasars either appear or disappear on timescales of years (e.g., LaMassa et al. 2015; MacLeod et al. 2016; Gezari et al. 2017; Yang et al. 2018). The physical processes causing these changing-look phenomena are hotly debated, but the physical changes in the accretion disk is the likely cause rather than changes in obscuration (e.g., LaMassa et al. 2017; Lawrence 2018; Dexter & Begelman 2019).

Stern et al. (2018) recently discovered one changing-look quasar, WISE J1052+1519, and carefully discussed the possible disk timescales matching the year timescale. They found that the dynamical timescale is several weeks, which is therefore too short, whereas the viscous timescale, which would be responsible for the luminosity change of dying AGN, is far too long. Instead, a few-years-long thermal timescale would be a plausible one, matching the observed year scale variability. The similar origin is also proposed for a different changing-look AGN Mrk 1018 (Noda & Done 2018). Therefore, both dying and changing-look AGNs show the luminosity change, but their luminosity changes are likely based on the different physical mechanisms of the accretion disk. Those property differences between dying AGNs and changing-look quasars are also summarized in Table 3.

3.5. Comparison between Dying AGN and Remnant Radio Sources

Our study suggests that the absence of radio core at the center of galaxies would be a good indicator for searching for a dying AGNs. Although they are very rare, some authors have already found candidates of radio galaxies without clear radio core signs, or so-called remnant radio sources. Cordey (1987) showed that IC 2476 has double radio lobes with a separation of 560 kpc, but without a clear radio core at the location of the host galaxy. In addition, Dwarakanath & Kale (2009) have conducted a search for remnant radio sources using VLA 74 MHz survey (VLSS; 80 arcsec spatial resolution) and NRAO VLA Sky Survey (NVSS; 45 arcsec spatial resolution) through the search of very steep radio sources whose spectral index is $\alpha < -1.8$ (where $f_\nu \propto \nu^\alpha$) between 74 MHz and 1.4 GHz. Of the $\sim 10^4$ parent sample, they found 10 such candidates and the spectral age estimation of jet lobes gives the fading age of >10 Myr.

The timescale found in remnant radio sources is at least two orders of magnitude longer than the fading phase traced for Arp 187. This discrepancy is natural because their steep spectral selection method is sensitive to longer jet age with $>10^7$ yr at the frequency of ~ 100 MHz (e.g., Jamrozny et al. 2008) and their moderate spectral resolution of 80 arcsec is equivalent to the physical angular size of ~ 260 kpc, or the corresponding kinematic age of $t_{\text{dyn}} \sim 8 \times 10^6$ yr at $z \sim 0.2$, where most of the samples are found. Thus, previous radio studies are sensitive to trace much longer AGN activities with >10 Myr. Considering the typical quasar lifetime of ~ 30 Myr (e.g., Hopkins et al. 2006; Inayoshi et al. 2018), remnant radio sources are more suitable to trace a comparable timescale of the

AGN lifetime rather than the AGN fading timescale traced in this study.

Recently, higher spatial resolution surveys are ongoing using Low-Frequency Array (LOFAR; van Haarlem et al. 2013). LOFAR covers the largely unexplored low-frequency range between 10–240 MHz, and has the resolution of ~ 6 arcsec at 150 MHz. This would give an opportunity to search for smaller, which is equivalent to younger, dying radio sources at the age of ~ 1 Myr. The initial-stage surveys have already found new remnant radio source candidates (e.g., Mahatma et al. 2018), and future LOFAR surveys would give us a more statistically significant number of such younger remnant radio sources and would help to create a more complete picture of both of AGN lifetime and dying phase (also see a recent review by Morganti 2017).

3.6. Future Observations

There is some room for the further constraints of the AGN activities of Arp 187. *JWST*/MIRI will give us the nuclear MIR spectra with the least host galaxy contamination with great sensitivity. The X-ray satellite *NuSTAR* is going to constrain the current AGN activity. Recently, thanks to the great sensitivity at $E > 10$ keV, *NuSTAR* revealed that a fading AGN candidate in IC 2497 is actually a Compton-thick AGN (Sartori et al. 2018a), whose nuclear X-ray emission could not be discovered in the previous X-ray satellites such as *Chandra*, *XMM/Newton*, and even with *Suzaku* (Schawinski et al. 2010). Although the same discovery is unlikely for Arp 187, because the MIR emission is known to be considerably weak, *NuSTAR* will constrain the nuclear activity down to $\log(L_{2-10}/\text{erg s}^{-1}) \simeq 42$ even with the Compton-thick absorption of $\log N_{\text{H}} \simeq 24.3$. Finally, the optical or near-IR IFU will also give us the detailed NLR size which is poorly constrained with the current study.

4. Conclusion

We have compiled the multiwavelength AGN signatures of dying AGN candidate Arp 187, on the basis of the combinations of the newly conducted ALMA observations and the archival VLA 5–10 GHz data, 6dF optical spectrum, NEOWISE, and ALLWISE IR data. Our results show that the AGN in Arp 187 is a bona fide dying AGN, whose central engine is already dead, but the large-scale AGN indicators are still observable as the remnant of the past AGN activity. The central engine of Arp 187 has experienced the drastic luminosity decline by a factor of 10^{3-5} within the last 10^4 yr. Our rough estimation suggests that the viscous timescale most closely matches the obtained timescale in this study. This supports that Arp 187 has been in a later fading phase whose UV-emitting region in the accretion disk is likely to be almost disappeared, whereas other fading AGNs show clear signs that the UV-emitting region is still alive.

We thank the anonymous referee who offered a positive and helpful report. We thank Kazunori Akiyama, Luca Comisso, Kohei Inayoshi, Masatoshi Imanishi, Mitsuru Kokubo, Hiroshi Nagai, and Hirofumi Noda for fruitful discussions. We also would like to thank Jaejin Shin for giving us the spectral fitting result of the optical spectrum.

This paper makes use of the following ALMA data: ADS/JAO.ALMA#2015.1.01005.S. ALMA is a partnership of ESO (representing its member states), NSF (USA) and NINS

(Japan), together with NRC (Canada) and NSC and ASIAA (Taiwan) and KASI (Republic of Korea), in cooperation with the Republic of Chile. The Joint ALMA Observatory is operated by ESO, AUI/NRAO and NAOJ. In addition, this paper includes observational material taken with VLA, which is one of the NRAO instruments. The National Radio Astronomy Observatory is a facility of the National Science Foundation operated under cooperative agreement by Associated Universities, Inc. This paper also makes use of data products from the *WISE*, which is a joint project of the University of California, Los Angeles, and the Jet Propulsion Laboratory/California Institute of Technology, funded by the National Aeronautics and Space Administration.

This work is supported by Program for Establishing a Consortium for the Development of Human Resources in Science and Technology, Japan Science and Technology Agency (JST) and is partially supported by Japan Society for the Promotion of Science (JSPS) KAKENHI (18K13584; KI, 18J01050; YT, 16K17672; MS). K.M. is supported by JSPS Overseas Research Fellowships.

Facilities: ALMA, VLA, *WISE*, *Spitzer*, *Chandra*, *XMM-Newton*, *Swift*/BAT.

Software: astropy (Astropy Collaboration et al. 2013), Matplotlib (Hunter 2007), Pandas (McKinney 2010).


ORCID iDs

Kohei Ichikawa  <https://orcid.org/0000-0002-4377-903X>

Hyun-Jin Bae  <https://orcid.org/0000-0001-5134-5517>

Taiki Kawamuro  <https://orcid.org/0000-0002-6808-2052>

Kenta Matsuoka  <https://orcid.org/0000-0002-2689-4634>

Yoshiki Toba  <https://orcid.org/0000-0002-3531-7863>

References

- Abazajian, K. N., Adelman-McCarthy, J. K., Agüeros, M. A., et al. 2009, *ApJS*, 182, 543
- Alexander, D. M., & Hickox, R. C. 2012, *NewAR*, 56, 93
- Alloin, D., Pelat, D., Phillips, M., & Whittle, M. 1985, *ApJ*, 288, 205
- Antonucci, R. 1993, *ARA&A*, 31, 473
- Antonucci, R. R. J., & Cohen, R. D. 1983, *ApJ*, 271, 564
- Asmus, D., Gandhi, P., Hönl, S. F., Smette, A., & Duschl, W. J. 2015, *MNRAS*, 454, 766
- Astropy Collaboration, Robitaille, T. P., Tollerud, E. J., et al. 2013, *A&A*, 558, A33
- Bae, H.-J., Woo, J.-H., Karouzos, M., et al. 2017, *ApJ*, 837, 91
- Bennert, N., Falcke, H., Schulz, H., Wilson, A. S., & Wills, B. J. 2002, *ApJL*, 574, L105
- Bennert, N., Jungwiert, B., Komossa, S., Haas, M., & Chini, R. 2006, *A&A*, 456, 953
- Berney, S., Koss, M., Trakhtenbrot, B., et al. 2015, *MNRAS*, 454, 3622
- Blandford, R. D., & Königl, A. 1979, *ApJ*, 232, 34
- Calzetti, D., Kinney, A. L., & Storchi-Bergmann, T. 1994, *ApJ*, 429, 582
- Cordey, R. A. 1987, *MNRAS*, 227, 695
- Czerny, B. 2006, in ASP Conf. Ser. 360, AGN Variability from X-Rays to Radio Waves, ed. C. M. Gaskell et al. (San Francisco, CA: ASP), 265
- Davis, S. W., Stone, J. M., & Pessah, M. E. 2010, *ApJ*, 713, 52
- Dexter, J., & Begelman, M. C. 2019, *MNRAS*, 483, L17
- Domínguez, A., Siana, B., Henry, A. L., et al. 2013, *ApJ*, 763, 145
- Dwarakanath, K. S., & Kale, R. 2009, *ApJL*, 698, L163
- Evans, I. N., Primini, F. A., Glotfelty, K. J., et al. 2010, *ApJS*, 189, 37
- Falcke, H., Körding, E., & Markoff, S. 2004, *A&A*, 414, 895
- Fraquelli, H. A., Storchi-Bergmann, T., & Levenson, N. A. 2003, *MNRAS*, 341, 449
- Gandhi, P., Horst, H., Smette, A., et al. 2009, *A&A*, 502, 457
- Gezari, S., Hung, T., Cenko, S. B., et al. 2017, *ApJ*, 835, 144
- Godfrey, L. E. H., Morganti, R., & Brienza, M. 2017, *MNRAS*, 471, 891
- Greene, J. E., Zakamska, N. L., Ho, L. C., & Barth, A. J. 2011, *ApJ*, 732, 9
- Hada, K., Doi, A., Kino, M., et al. 2011, *Natur*, 477, 185
- Hainline, K. N., Hickox, R., Greene, J. E., Myers, A. D., & Zakamska, N. L. 2013, *ApJ*, 774, 145
- Heckman, T. M., Kauffmann, G., Brinchmann, J., et al. 2004, *ApJ*, 613, 109
- Heckman, T. M., Ptak, A., Hornschemeier, A., & Kauffmann, G. 2005, *ApJ*, 634, 161
- Hirose, S., Blaes, O., & Krolik, J. H. 2009, *ApJ*, 704, 781
- Hopkins, P. F., Hernquist, L., Cox, T. J., et al. 2006, *ApJS*, 163, 1
- Humphrey, A., Villar-Martín, M., Sánchez, S. F., et al. 2010, *MNRAS*, 408, L1
- Hunter, J. D. 2007, *CSE*, 9, 90
- Husemann, B., Wisotzki, L., Sánchez, S. F., & Jahnke, K. 2013, *A&A*, 549, A43
- Ichikawa, K., Imanishi, M., Ueda, Y., et al. 2014, *ApJ*, 794, 139
- Ichikawa, K., & Inayoshi, K. 2017, *ApJL*, 840, L9
- Ichikawa, K., Ricci, C., Ueda, Y., et al. 2017, *ApJ*, 835, 74
- Ichikawa, K., Ricci, C., Ueda, Y., et al. 2019, *ApJ*, 870, 16
- Ichikawa, K., & Tazaki, R. 2017, *ApJ*, 844, 21
- Ichikawa, K., Ueda, J., Shidatsu, M., Kawamuro, T., & Matsuoka, K. 2016, *PASJ*, 68, 9
- Ichikawa, K., Ueda, Y., Terashima, Y., et al. 2012, *ApJ*, 754, 45
- Inayoshi, K., & Haiman, Z. 2016, *ApJ*, 828, 110
- Inayoshi, K., Ichikawa, K., & Haiman, Z. 2018, *ApJL*, 863, L36
- Jamroz, M., Konar, C., Machalski, J., & Saikia, D. J. 2008, *MNRAS*, 385, 1286
- Jones, D. H., Read, M. A., Saunders, W., et al. 2009, *MNRAS*, 399, 683
- Józsa, G. I. G., Garrett, M. A., Oosterloo, T. A., et al. 2009, *A&A*, 500, L33
- Jun, H. D., Im, M., Lee, H. M., et al. 2015, *ApJ*, 806, 109
- Karouzos, M., Woo, J.-H., & Bae, H.-J. 2016, *ApJ*, 819, 148
- Kato, S., Fukue, J., & Mineshige, S. 2008, Black-Hole Accretion Disks—Towards a New Paradigm (Kyoto, Japan), 549
- Kauffmann, G., Heckman, T. M., Tremonti, C., et al. 2003, *MNRAS*, 346, 1055
- Kawamuro, T., Schirmer, M., Turner, J. E. H., Davies, R. L., & Ichikawa, K. 2017, *ApJ*, 848, 42
- Keel, W. C., Lintott, C. J., Maksym, W. P., et al. 2017, *ApJ*, 835, 256
- Keel, W. C., Lintott, C. J., Schawinski, K., et al. 2012, *AJ*, 144, 66
- Keel, W. C., Maksym, W. P., Bennert, V. N., et al. 2015, *AJ*, 149, 155
- Kewley, L. J., Dopita, M. A., Sutherland, R. S., Heisler, C. A., & Trevena, J. 2001, *ApJ*, 556, 121
- Kewley, L. J., Groves, B., Kauffmann, G., & Heckman, T. 2006, *MNRAS*, 372, 961
- Komossa, S., Xu, D., Zhou, H., Storchi-Bergmann, T., & Binette, L. 2008, *ApJ*, 680, 926
- Kormendy, J., & Ho, L. C. 2013, *ARA&A*, 51, 511
- LaMassa, S. M., Cales, S., Moran, E. C., et al. 2015, *ApJ*, 800, 144
- LaMassa, S. M., Heckman, T. M., Ptak, A., et al. 2010, *ApJ*, 720, 786
- LaMassa, S. M., Heckman, T. M., Ptak, A., & Urry, C. M. 2013, *ApJL*, 765, L33
- LaMassa, S. M., Yaqoob, T., & Kilgard, R. 2017, *ApJ*, 840, 11
- Lawrence, A. 2018, *NatAs*, 2, 102
- Lintott, C. J., Schawinski, K., Keel, W., et al. 2009, *MNRAS*, 399, 129
- Liu, G., Zakamska, N. L., Greene, J. E., Nesvadba, N. P. H., & Liu, X. 2013, *MNRAS*, 436, 2576
- MacLeod, C. L., Ross, N. P., Lawrence, A., et al. 2016, *MNRAS*, 457, 389
- Mahatma, V. H., Hardcastle, M. J., Williams, W. L., et al. 2018, *MNRAS*, 475, A457
- Mainzer, A., Bauer, J., Cutri, R. M., et al. 2014, *ApJ*, 792, 30
- Mainzer, A., Bauer, J., Grav, T., et al. 2011, *ApJ*, 731, 53
- Malkan, M. A., & Sargent, W. L. W. 1982, *ApJ*, 254, 22
- Marconi, A., Risaliti, G., Gilli, R., et al. 2004, *MNRAS*, 351, 169
- Markwardt, C. B. 2009, in ASP Conf. Ser. 411, Astronomical Data Analysis Software and Systems XVIII, ed. D. A. Bohlender, D. Durand, & P. Dowler (San Francisco, CA: ASP), 251
- Mateos, S., Alonso-Herrero, A., Carrera, F. J., et al. 2012, *MNRAS*, 426, 3271
- Mateos, S., Carrera, F. J., Alonso-Herrero, A., et al. 2015, *MNRAS*, 449, 1422
- Matsuoka, K., & Woo, J.-H. 2015, *ApJ*, 807, 28
- McConnell, N. J., Ma, C.-P., Gebhardt, K., et al. 2011, *Natur*, 480, 215
- McKinney, W. 2010, in Proc. 9th Python in Science Conf., Data Structures for Statistical Computing in Python, ed. S. van der Walt & J. Millman, 51, <http://conference.scipy.org/proceedings/scipy2010/mckinney.html>
- McLure, R. J., & Dunlop, J. S. 2004, *MNRAS*, 352, 1390
- Merloni, M., Heinz, S., & di Matteo, T. 2003, *MNRAS*, 345, 1057
- Morganti, R. 2017, *NatAs*, 1, 596
- Murgia, M., Fanti, C., Fanti, R., et al. 1999, *A&A*, 345, 769
- Nagai, H., Inoue, M., Asada, K., Kameno, S., & Doi, A. 2006, *ApJ*, 648, 148
- Nagar, N. M., Oliva, E., Marconi, A., & Maiolino, R. 2002, *A&A*, 391, L21
- Netzer, H. 2003, *ApJL*, 583, L5
- Netzer, H. 2009, *MNRAS*, 399, 1907
- Netzer, H., Mainieri, V., Rosati, P., & Trakhtenbrot, B. 2006, *A&A*, 453, 525
- Noda, H., & Done, C. 2018, *MNRAS*, 480, 3898

- Novak, G. S., Ostriker, J. P., & Ciotti, L. 2011, *ApJ*, 737, 26
- Oh, K., Koss, M., Markwardt, C. B., et al. 2018, *ApJS*, 235, 4
- Panessa, F., Bassani, L., Cappi, M., et al. 2006, *A&A*, 455, 173
- Ricci, C., Trakhtenbrot, B., Koss, M. J., et al. 2017a, *ApJS*, 233, 17
- Ricci, C., Trakhtenbrot, B., Koss, M. J., et al. 2017b, *Natur*, 549, 488
- Ricci, C., Ueda, Y., Koss, M. J., et al. 2015, *ApJL*, 815, L13
- Rigby, J. R., Diamond-Stanic, A. M., & Aniano, G. 2009, *ApJ*, 700, 1878
- Rosen, S. R., Webb, N. A., Watson, M. G., et al. 2016, *A&A*, 590, A1
- Ross, N. P., Ford, K. E. S., Graham, M., et al. 2018, *MNRAS*, 480, 4468
- Rothberg, B., & Joseph, R. D. 2004, *AJ*, 128, 2098
- Ruan, J. J., Anderson, S. F., Cales, S. L., et al. 2016, *ApJ*, 826, 188
- Runnoe, J. C., Cales, S., Ruan, J. J., et al. 2016, *MNRAS*, 455, 1691
- Saikia, D. J., & Jamroz, M. 2009, *BASI*, 37, arXiv:1002.1841
- Sánchez-Blázquez, P., Peletier, R. F., Jiménez-Vicente, J., et al. 2006, *MNRAS*, 371, 703
- Sartori, L. F., Schawinski, K., Koss, M. J., et al. 2018a, *MNRAS*, 474, 2444
- Sartori, L. F., Schawinski, K., Trakhtenbrot, B., et al. 2018b, *MNRAS*, 476, L34
- Schawinski, K., Evans, D. A., Virani, S., et al. 2010, *ApJL*, 724, L30
- Schawinski, K., Koss, M., Berney, S., & Sartori, L. F. 2015, *MNRAS*, 451, 2517
- Schirmer, M., Diaz, R., Holmberg, K., Levenson, N. A., & Winge, C. 2013, *ApJ*, 763, 60
- Schirmer, M., Malhotra, S., Levenson, N. A., et al. 2016, *MNRAS*, 463, 1554
- Schmitt, H. R., Donley, J. L., Antonucci, R. R. J., et al. 2003, *ApJ*, 597, 768
- Schweizer, F., Seitzer, P., Kelson, D. D., Villanueva, E. V., & Walth, G. L. 2013, *ApJ*, 773, 148
- Shakura, N. I., & Sunyaev, R. A. 1973, *A&A*, 24, 337
- Shen, Y., Richards, G. T., Strauss, M. A., et al. 2011, *ApJS*, 194, 45
- Soltan, A. 1982, *MNRAS*, 200, 115
- Stern, D., Assef, R. J., Benford, D. J., et al. 2012, *ApJ*, 753, 30
- Stern, D., McKernan, B., Graham, M. J., et al. 2018, *ApJ*, 864, 27
- Toba, Y., Bae, H.-J., Nagao, T., et al. 2017, *ApJ*, 850, 140
- Toba, Y., Oyabu, S., Matsuhara, H., et al. 2014, *ApJ*, 788, 45
- Tohline, J. E., & Osterbrock, D. E. 1976, *ApJL*, 210, L117
- Trakhtenbrot, B. 2014, *ApJL*, 789, L9
- Ueda, J., Iono, D., Yun, M. S., et al. 2014, *ApJS*, 214, 1
- Ueda, Y., Hashimoto, Y., Ichikawa, K., et al. 2015, *ApJ*, 815, 1
- van Haarlem, M. P., Wise, M. W., Gunst, A. W., et al. 2013, *A&A*, 556, A2
- Vanden Berk, D. E., Richards, G. T., Bauer, A., et al. 2001, *AJ*, 122, 549
- Veilleux, S., & Osterbrock, D. E. 1987, *ApJS*, 63, 295
- Villar-Martín, M., Cabrera-Lavers, A., Humphrey, A., et al. 2018, *MNRAS*, 474, 2302
- Voges, W., Aschenbach, B., Boller, T., et al. 1999, *A&A*, 349, 389
- Wright, E. L., Eisenhardt, P. R. M., Mainzer, A. K., et al. 2010, *AJ*, 140, 1868
- Wu, X.-B., Wang, F., Fan, X., et al. 2015, *Natur*, 518, 512
- Wylezalek, D., Zakamska, N. L., Greene, J. E., et al. 2018, *MNRAS*, 474, 1499
- Yang, Q., Wu, X.-B., Fan, X., et al. 2018, *ApJ*, 862, 109
- Yu, Q., & Tremaine, S. 2002, *MNRAS*, 335, 965
- Yuan, F., & Cui, W. 2005, *ApJ*, 629, 408
- Yuan, F., & Narayan, R. 2014, *ARA&A*, 52, 529